

Accepted by ApJ

Insights into the carbon chemistry of Mon R2

J. R. Rizzo

*Departamento de Física, Universidad Europea de Madrid, Urb. El Bosque, Tajo s/n,
E-28670 Villaviciosa de Odón, Spain*

jricardo.rizzo@uem.es

A. Fuente and S. García-Burillo

Observatorio Astronómico Nacional, Aptdo. Correos 112, E-28803 Alcalá de Henares, Spain

ABSTRACT

Aiming to learn about the chemistry of the dense PDR around the ultracompact (UC) H II region in Mon R2, we have observed a series of mm-wavelength transitions of C₃H₂ and C₂H. In addition, we have traced the distribution of other molecules, such as H¹³CO⁺, SiO, HCO, and HC₃N. These data, together with the reactive ions recently detected, have been considered to determine the physical conditions and to model the PDR chemistry. We then identified two kind of molecules. The first group, formed by the reactive ions (CO⁺, HOC⁺) and small hydrocarbons (C₂H, C₃H₂), traces the surface layers of the PDR and is presumably exposed to a high UV field (hence we called it as “*high UV*”, or HUV). HUV species is expected to dominate for visual absorptions $2 < A_V < 5$ mag. A second group (less exposed to the UV field, and hence called “*low UV*”, or LUV) includes HCO and SiO, and is mainly present at the edges of the PDR ($A_V > 5$ mag). While the abundances of the HUV molecules can be explained by gas phase models, this is not the case for the studied LUV ones. Although some efficient gas-phase reactions might be lacking, grain chemistry sounds like a probable mechanism able to explain the observed enhancement of HCO and SiO. Within this scenario, the interaction of UV photons with grains produces an important effect on the molecular gas chemistry and constitutes the first evidence of an ionization front created by the UC H II region carving its host molecular cloud. The physical conditions and kinematics of the gas layer which surrounds the UC H II region were derived from the HUV molecules. Molecular hydrogen densities $> 4 \cdot 10^6 \text{ cm}^{-3}$ are required to reproduce the observations. Such high densities suggest that the H II region could be pressure-confined by the surrounding high density molecular gas.

Subject headings: ISM: abundances — ISM: H II regions — ISM: individual(Mon R2) — ISM: molecules — Stars: formation

1. Introduction

Mon R2 is a nearby ($D = 830$ pc; Herbst & Racine 1976) complex star forming region. It hosts an ultracompact (UC) HII region near its center, powered by the infrared source Mon R2 IRS 1. The molecular content of this region has been the subject of several observational studies in the last decade. So far, it is known a huge CO bipolar outflow (Meyers-Rice & Lada 1991), $\sim 15'$ long ($= 3.6$ pc), which is probably a relic of the formation of the B0V star associated to IRS1 (Massi, Felli, & Simon 1985; Henning, Chini, & Pfau 1992).

Mon R2 is an excellent laboratory to learn about the physical conditions and kinematics of an extreme PDR ($G_0 = 5 \cdot 10^5$ in units of Habing field, Rizzo et al. 2003). Continuum observations at 6cm, reported by Wood & Churchwell (1989), show that the UC HII region is highly asymmetric, has a cometary shape and reaches its maximum toward its exciting star, Mon R2 IRS 1. The CS 7→6 emission map from Choi et al. (2000) shows that the UC HII region is located inside a cavity and bound by a dense molecular ridge (see Fig. 1). This picture is consistent with infrared images of the region, which show an almost spherical distribution of hot dust surrounded by the molecular cloud.

The physical and chemical conditions of the PDRs associated to UC HII regions remain not enough known, mainly due to important observational problems: (a) These PDRs are too thin to be resolved by single-dish telescopes; (b) They are usually located in very complex star-forming regions, where confusion with the parent molecular cloud, hot cores, and outflows may be considerable. The study requires specific PDR tracers which allow us to separate their emission from other sources.

Reactive ions and small hydrocarbons have been proposed as abundant species, which may trace the hot ionized/molecular gas interface (Sternberg & Dalgarno 1995). The detection of the reactive ions CO^+ and HOC^+ is almost unambiguously associated to regions with a high ionizing flux, either PDRs or XDRs (Fuente et al. 2003; Rizzo et al. 2003; Usero et al. 2004; Savage & Ziurys 2004). In the case of Mon R2, Rizzo et al. (2003) have recently reported the detection of the reactive ions CO^+ and HOC^+ towards the peak of the UC HII region. In addition to chemical arguments, both the morphology and velocity profile of the lines suggested a link between the HII region and these species. Both ions were detected towards the peak of the UC HII regions and remain undetected in the molecular cloud. Furthermore, the velocity profile of these lines is different from those of other dense gas tracers.

The reactive ions have an intense emission peak at 10.5 km s^{-1} which is not detected in the other molecules observed. Therefore, the emission of this velocity component may arise in narrow layers of molecular gas surrounding the HII region, where the chemistry is dominated by UV photons.

Small hydrocarbons have enhanced abundances in PDRs (Fuente et al. 2003, 2005; Teyssier et al. 2004; Pety et al. 2005). In particular, Teyssier et al. (2004) have detected c-C₃H₂ and C₄H towards the Horsehead nebula with an abundance one order of magnitude larger than that predicted by gas-phase PDR models. This is clearly seen by comparing the [c-C₃H₂]/[HC₃N] ratio in PDRs and dark clouds. While both species have similar abundances in dark clouds, the [c-C₃H₂]/[HC₃N] ratio is above 10 in PDRs. Since both molecules are easily destroyed by photodissociation, this suggests the existence of an additional c-C₃H₂ formation mechanism in PDRs.

Enhanced abundances of some other compounds have also been related to the presence of intense UV fields into molecular clouds. Schenewerk et al. (1988) measured a value of $[\text{HCO}]/[\text{H}^{13}\text{CO}^+] = 9.7$ in the H II region NGC 2024. However, the same authors report values significantly lower than 1 –i.e., an order magnitude below those found in NGC 2024– in Galactic clouds without developed H II regions, or having no indication of star formation. More recently, Schilke et al. (2001) have searched for HCO in a reduced sample of prototypical PDRs; the estimated $[\text{HCO}]/[\text{H}^{13}\text{CO}^+]$ abundance ratios range from 30 (in the Orion bar) to 3 (in NGC 7023). The largest HCO abundances are found in the Orion bar, the paradigm of interaction between an H II region (M42) and its parent molecular cloud. García-Burillo et al. (2002) obtained a high angular resolution image showing widespread HCO emission in the external galaxy M82. The enhanced HCO abundance ($[\text{HCO}]/[\text{H}^{13}\text{CO}^+] \sim 3.6$) measured across the whole M82 disk was also interpreted in terms of a giant PDR of 650 pc size.

SiO is known to be a privileged tracer of large-scale shocks in the interstellar medium (Martín-Pintado et al. 1997; García-Burillo et al. 2000, 2001). Its fractional abundance is enhanced by more than 3 orders of magnitude in shocked regions relative to its abundance in quiescent clouds where it takes values $\leq 10^{-12}$. Schilke et al. (2001) observed SiO towards a sample of PDRs and obtain fractional abundances of $\sim 10^{-11}$ in these regions, i.e., a factor of 10 larger than that in dark clouds.

In this paper, we present observations of a selected set of molecular species (C₂H, c-C₃H₂, HC₃N, H¹³CO⁺, HCO, and SiO) which are thought to be good probes of the different layers of the molecular gas in PDRs. In this way, we have performed a study of the physical conditions, the chemistry, and the kinematics of the molecular gas surrounding the UC HII region.

2. Observations

The observations were carried out using the IRAM 30m radio telescope in Pico de Veleta (Spain) during July 2002 and August 2003. The multi-receiver capability of the telescope was used for these observations. The observed rotational transitions, frequencies, beam sizes, and main-beam efficiencies are shown in Table 1. The backends used for the observations were an autocorrelator split in several parts, a 256×100 kHz and two 512×1 MHz filter-banks. All the lines but $\text{H}^{13}\text{CO}^+ 1 \rightarrow 0$ and $\text{C}_3\text{H}_2 5(1,4) \rightarrow 4(2,3)$ have been measured with two spectral resolutions, namely the lower spectral resolution provided by the 1 MHz filter-bank and the higher one, 78 kHz–100 kHz, provided by the autocorrelator and the 100 kHz filter bank. The $\text{H}^{13}\text{CO}^+ 1 \rightarrow 0$ and $\text{C}_3\text{H}_2 5(1,4) \rightarrow 4(2,3)$ lines have only been measured with the 1 MHz filter-bank, providing the lower spectral resolution. The $\text{C}_3\text{H}_2 6(1,6) \rightarrow 5(0,5)$ [ortho] and $6(0,6) \rightarrow 5(1,5)$ [para] are blended.

The observational strategy was as follows. We have mapped the UC H II region Mon R2 and its surroundings in millimeter transitions of H^{13}CO^+ , HC_3N , HCO , and SiO . The C_2H and C_3H_2 transitions were observed along a strip transversal to the UC H II region, at an inclination angle (east to north) of 135° , which is approximately the symmetry axis of Mon R2. The mapped area ($72'' \times 72''$) and strip positions are sketched in Fig. 1, overlaid on the CS $7 \rightarrow 6$ map of Choi et al. (2000) and the 6 cm-continuum map of Wood & Churchwell (1989). The relative offsets are referred to Mon R2 IRS1, (RA, Dec.)₂₀₀₀ = ($06^{\text{h}}07^{\text{m}}46^{\text{s}}.2$, $-06^\circ23'08''.3$). Longer integration time was devoted to observe two particular positions: the maximum of the continuum emission, at $(0'', 0'')$, and the maximum of the molecular envelope, at $(+10'', -10'')$. These two positions were also observed in the reactive ions CO^+ and HOC^+ , and already published in a recent paper (Rizzo et al. 2003).

3. Results

3.1. C_3H_2 and C_2H along the strip

The small hydrocarbons C_2H and C_3H_2 have been observed along a strip crossing the ionization bar in Mon R2. After the hyperfine-structure analysis –which compares the relative intensities of each component–, we have found that the C_2H triplet emission at 87.3 GHz is optically thin at all positions. Based on this result, we will deal in the following just with the most intense hyperfine component ($F = 2 - 1$), referring to this as “the $\text{C}_2\text{H} 1 \rightarrow 0$ line”. Some of the C_2H and C_3H_2 observed spectra are shown in Fig. 2. The Gaussian fits to a single component are also shown in Table 2 for all the lines. The $\text{C}_2\text{H} 1 \rightarrow 0$ line shows emission at high velocities ($V_{\text{LSR}} < 8 \text{ km s}^{-1}$ and $V_{\text{LSR}} > 12 \text{ km s}^{-1}$) that is not detected (or

only marginally detected) in the C_3H_2 lines. These velocity ranges coincide with those of the red-shifted and blue-shifted emission in the large-scale, now inactive, outflow associated with IRS 1 (Meyers-Rice & Lada 1991; Giannakopoulou et al. 1997). We have not detected emission at high velocity in any other of the PDR tracers studied in this paper and Rizzo et al. (2003). Thus, we consider that the high velocity C_2H emission is not related to the UC H II region but to the low density gas that share the kinematics of the large-scale outflow. Since we are mainly interested in the study of the PDR surrounding the UC H II region, we have only used the C_2H emission in the range $8\text{--}12 \text{ km s}^{-1}$ in our calculations.

Within the considered velocity range, the velocities and spatial distribution of the C_2H $1\rightarrow 0$ and C_3H_2 $2\rightarrow 1$ lines are remarkable similar, which suggest that both lines trace essentially the same region. However, the emission of the C_3H_2 $2\rightarrow 1$ and the C_3H_2 $6\rightarrow 5$ lines have different kinematics and spatial distribution, which became eloquent when looking at the central velocities in Table 2 and the shaded areas in Fig. 2. The C_3H_2 $2\rightarrow 1$ line is narrower than the $6\rightarrow 5$ line along the whole strip. Furthermore, the central velocity of the $2\rightarrow 1$ line is lower than that of the $6\rightarrow 5$ line towards the UC H II region. When looking at the areas, it is remarkable the different spatial distribution of the $2\rightarrow 1$ and $6\rightarrow 5$ lines. The $2\rightarrow 1$ emission (a low excitation line) is clearly lower at the central part of the strip, while the $6\rightarrow 5$ emission (a high excitation line) is particularly intense there.

This behavior is better explained by assuming the existence of *at least* two gas components characterized by different velocities. The blue velocity component (hereafter referred to as C1), emitting at velocities from ≈ 8 to 10 km s^{-1} , is dominated by the emission of the $2\rightarrow 1$ line along the whole strip, but it is not particularly intense in the $6\rightarrow 5$ line. This component remains quite uniform along the strip. The red velocity component, with emission from ≈ 10 to 12 km s^{-1} and hereafter referred to as C2, has intense emission in the $6\rightarrow 5$ line but it is very weak in the $2\rightarrow 1$ line. C2 is especially intense towards the inner H II region. The distribution of both components can be interpreted as C1 associated with the foreground molecular cloud and C2 associated with the H II region, or the interface between it and the molecular cloud.

This trend is illustrated in Fig. 3, where we plot the integrated intensity of the C_3H_2 $6\rightarrow 5$ line (Fig. 3a) and the $6\rightarrow 5/2\rightarrow 1$ line intensity ratio (hereafter referred to as R_{62}) for each component (Fig. 3b). R_{62} remains quite constant and ~ 1 for C1 along the strip. However, it has significant variations in C2. The values of R_{62} are ~ 0.6 outside the UC H II region and > 4 towards the inner region. The Fig. 3b clearly separates both components, and shows that C2 is tracing highly excited molecular gas, linked to the UC H II region. This splitting of the values of R_{62} is also in agreement with the spatial distribution of both components.

Of course, the different beams involved in both lines affect the computation of R_{62} . We could estimate the beam dilution by convolving the C_3H_2 6→5 emission of the C2 down to the angular resolution of the 2→1 line. This one-dimensional smoothing was performed along the symmetry axis, which shows the largest variations in other molecular tracers. The results are shown by dashed lines in Fig. 3. As expected, the distribution of the 6→5 line intensity peaks in the southeastern border of the UC H II region. Furthermore, it is remarkable that R_{62} remains > 5 in the three central positions. In other words, the high value of R_{62} there, even smoothed, strengthens the mutual relationship between C2 and the UC H II region.

3.2. Maps

We have mapped the region indicated in Fig. 1 in several rotational lines. Fig. 4 shows the resultant maps in $H^{13}CO^+$ 1→0 (Fig. 4a), SiO 2→1 (Fig. 4b), HCO 1→0 (Fig. 4c), and HC_3N 10→9 (Fig. 4d). Superimposed are the 6 cm-continuum emission from Wood & Churchwell (1989). All the maps were constructed by integrating the lines along the total velocity range of emission. We note remarkable differences in the distribution of the different species. The $H^{13}CO^+$ and the HC_3N emission clearly follow the high density gas, properly traced by the CS 7→6 emission (see Fig. 1) and reach a minimum toward the center of the UC H II region. This is consistent with the interpretation of $H^{13}CO^+$ and HC_3N as being photodissociated within the UC H II region.

However, the other molecules present different behaviors. The SiO and HCO emissions seem to be located preferably at intermediate positions between the molecular envelope and the H II region. Although this effect should be regarded as tentative, because the spatial difference between the continuum peak and the SiO distribution is about half a beam, the systematic difference looks evident, and clearly the SiO or HCO maps are different to those of $H^{13}CO^+$ or HC_3N . This result is in line with Schilke et al. (2001), who also found moderately enhanced SiO and HCO emissions close to the ionization front in the prototypical H II region M42. However, the two species peak at different positions. The HCO maxima appears almost exactly at the SiO minimum, and both emissions completely bound the inner UC H II region.

In Fig. 5 we show all the spectra we have observed towards the (0'',0'') position (this paper and Rizzo et al. 2003). The dashed vertical line traces the limits of C1 and C2. Unfortunately, some of the lines at (0'',0'') are rather weak, which yields a low S/N ratio. Even though, a quick look suggests the existence of two different behaviors in the shape of the observed lines. A first group of lines has the maximum intensity at velocities < 10 km s $^{-1}$, close to the C1 velocity; this is the case for the SiO and HCO lines. A second group peaks at velocities > 10 km s $^{-1}$ and are especially intense in C2; the C_3H_2 6→5, CO^+ 2→1

and $\text{HOC}^+ 1\rightarrow 0$ belongs to this group. The strong difference between the SiO lines at C2 velocities should be more carefully analyzed in future observations.

After a joint view of the maps (Fig. 4) and the spectra (Fig. 5), we see that the SiO and HCO emitting gas do not seem to share the same volume with the reactive ions and small hydrocarbons, but to arise in a more shielded layer of the PDR, which is preferably at the velocity of C1. As further discussed in Sects. 5 and 6, different excitation conditions and chemistry are associated to this shielded layer and C2.

4. Physical conditions: LVG results for the hydrocarbons

We have developed a LVG code to estimate the main physical parameters of the C_3H_2 molecule. The Einstein A-coefficients have been taken from Chandra (2003). The collisional rates are from Chandra & Kegel (2000), who provided values for kinetic temperatures (T_K) of 30, 60, 90, and 120 K. Our LVG code treats the ortho- and para- C_3H_2 as different species. In most positions, we have detected only the $2(1,2)\rightarrow 1(0,1)$ [ortho] and the $6\rightarrow 5$ (a blending of the $6(1,6)\rightarrow 5(0,5)$ [ortho] and $6(0,6)\rightarrow 5(1,5)$ [para]) lines. Then, we need to assume a value of the C_3H_2 ortho-to-para ratio (OTPR) in our calculations. In order to have an estimate of the OTPR, we have used the $6\rightarrow 5/5\rightarrow 4$ line intensity ratio (hereafter R_{65}) towards the $(0'',0'')$ and $(+10'',-10'')$ positions. The observed value, $R_{65} \sim 1.4 \pm 0.3$, is compatible with $R_{65} = 4/3$, which is expected for the standard value of 3. Therefore, we have assumed OTPR = 3 in our LVG calculations hereafter.

The LVG code was run for different sets of T_K , from 10 to 150 K. For T_K different to those tabulated by Chandra & Kegel (2000), we have interpolated or extrapolated between the two closest temperatures. A minimum value of 30 K for T_K is needed to reproduce the $6\rightarrow 5/2\rightarrow 1$ line ratio (hereafter referred to as R_{62}) both in C1 and C2. For $T_K > 50$ K, R_{62} is weakly dependent on the assumed kinetic temperature and traces mainly the hydrogen density. In Table 3, we show the LVG results assuming $T_K = 50$ K, the kinetic temperature derived by Giannakopoulou et al. (1997) from multiline molecular observations.

We have obtained rather uniform values of both the molecular density ($n(\text{H}_2)$) and the C_3H_2 column density ($N(\text{C}_3\text{H}_2)$) in C1 across the observed strip. The derived $n(\text{H}_2)$ is around $5 \cdot 10^5 \text{ cm}^{-3}$, in agreement with results derived from other tracers (Choi et al. 2000; Rizzo et al. 2003), and the $N(\text{C}_3\text{H}_2)$ are in the range $1\text{--}3 \cdot 10^{12} \text{ cm}^{-2}$. A different behavior is observed in C2. The C2 hydrogen density increases from a few 10^5 cm^{-3} outside the UC H II region to $> 4 \cdot 10^6 \text{ cm}^{-3}$ in the three central positions. This limit is almost insensitive to T_K in the range 50 to 150 K. Thus, the larger values of the R_{62} observed towards the H II region

cannot be due to a higher kinetic temperature. The Fig. 6 shows the LVG results from two of the runs, corresponding to values of T_K of 60 and 120 K. The shadowed areas indicate the range of observed values towards the (0", 0") position. While $N(C_3H_2)$ is similar in C1 and C2, the C2 density is a factor > 5 greater than in C1.

Recent results of Jaffe et al. (2003) and near-IR images show a shell-like structure, intense in mid- and near-IR, of a few arcsec width, wrapping up the UC H II region. It is indeed possible that C2 is tracing the *high density molecular gas* associated to this feature. This would also explain the spatial distribution of $N(C_3H_2)$ in C2 which slightly increases towards the border of the H II region, the expected behavior of a molecular shell surrounding the ionized gas.

We have estimated the C₂H column density ($N(C_2H)$) across the studied strip using the LVG code and assuming $n(H_2) = 10^6 \text{ cm}^{-3}$ and $T_K = 50 \text{ K}$. We have adopted the cross sections provided by Green & Thaddeus (1974) for the HCN molecule, and then used the IOS (Infinite-Order Sudden) approximation for molecular collision dynamics to get the collisional coefficients between different levels. A similar procedure was followed by Truong-Bach et al. (1987), who also provided the Einstein A- coefficients for C₂H.

The C1 and C2 components have been separated towards the (0", 0") and (+10", -10"). Most of the C₂H emission seem to be associated to C1 outwards these positions. The results are shown in Tables 3 and 4. $N(C_2H)$ varies from 2 to $4 \cdot 10^{14} \text{ cm}^{-2}$, decreasing toward the center of the H II region, as expected in a region where the molecules are photodestroyed by a high incident UV flux. When compared to C₃H₂, the $[C_3H_2]/[C_2H]$ ratio slightly increases towards the center; an exception is the last point of the strip, which has a considerable lower S/N ratio (see Table 3). Comparing both components, the $[C_3H_2]/[C_2H]$ ratio is three times greater in C2 than in C1 (see Table 4). As we will refer in Sect. 6.1, the significantly larger $[C_3H_2]/[C_2H]$ ratio in C2 reveals that the chemistry of the molecular gas is heavily affected by the UV radiation.

5. $H^{13}CO^+$, SiO and HC₃N fractional abundances

The $H^{13}CO^+$, SiO and HC₃N column densities have been estimated using an LVG code and assuming $T_K = 50 \text{ K}$ and $n(H_2) = 10^6 \text{ cm}^{-3}$. Under these physical conditions, the excitation temperature of the $H^{13}CO^+ 1 \rightarrow 0$ line is $\sim 20 \text{ K}$. We have also derived the HCO column density by assuming optically thin emission, LTE conditions and a rotation temperature of 20 K. The uncertainty in the excitation temperature of HCO should not affect the fractional abundances of these molecules. The results for some selected positions are shown in Table

5.

Significant changes in the fractional abundances are detected across the UC H II region. In particular, the HC_3N abundance decreases by a factor of ~ 3 towards the UC H II region ($X(\text{HC}_3\text{N}) \sim \text{a few } 10^{-10}$), when compared towards the dense molecular cloud (where $X(\text{HC}_3\text{N}) \sim 10^{-9}$). This decrease of the HC_3N abundance in regions of enhanced UV field has also been found in other regions like the prototypical PDR of the Orion Bar (Rodríguez-Franco et al. 1998), or the starburst galaxy M82 (Fuente et al. 2005), and it is easily explained by photodissociation.

SiO has a different behavior. The SiO abundance is low towards the center of the UC H II region ($X(\text{SiO}) \sim 5 \cdot 10^{-12}$). It is also low towards the dense molecular cloud, where we derive $X(\text{SiO}) < 7 \cdot 10^{-12}$, in agreement with the values of the SiO abundance measured in dark clouds. However, it is one order of magnitude higher at intermediate positions between the UC H II region and the molecular cloud; here, the SiO abundance is comparable to that found by Schilke et al. (2001) towards the PDRs associated with the Orion Bar and S140.

Similarly to SiO , the HCO abundance is also enhanced at the border of the UC H II region. In particular the $[\text{HCO}]/[\text{H}^{13}\text{CO}^+]$ ratio is 10 times larger in the position $(0'', 24'')$ than in the center of the UC H II region and in the dense molecular cloud. We have measured a HCO abundance as high as $\sim 10^{-9}$ towards the HCO peak. Such large values of the HCO abundance have been found at the border of the H II region NGC 2024 by Schenewerk et al. (1988) and in the Orion Bar by Schilke et al. (2001), suggesting that this molecule is specially abundant in the PDRs formed at the edges of the H II regions. García-Burillo et al. (2002) found large values of the HCO abundance in the starburst galaxy M82, where a low-density ionized component is filling a substantial fraction of its volume (see also Seaquist et al. 1996).

6. Photon-dominated chemistry in Mon R2

6.1. The surface layers of the PDR: HUV species

Our data show the existence of a high-density layer of gas associated to the UC H II region in Mon R2. This layer is traced by C2 and seems to have different physical conditions from that of C1 and the molecular cloud. Furthermore, a different chemistry may also carry out in the layer traced by C2. In order to explore this idea, we have computed the column densities and fractional abundances for the two components, towards the positions $(+10'', -10'')$ and $(0'', 0'')$, and for the molecules studied in this paper and Rizzo et al. (2003). The results are shown in Table 4. Significant differences exist between the $[\text{CO}^+]/[\text{HCO}^+]$,

$[\text{HCO}^+]/[\text{HOC}^+]$ and $[\text{C}_3\text{H}_2]/[\text{C}_2\text{H}]$ ratios between C1 and C2. In order to characterize the chemistry of the two components, we have modeled the PDR using the plane-parallel model developed by Le Bourlot and collaborators (Le Bourlot et al. 1993) with an UV field $G_0 = 5 \cdot 10^5$ in units of the Habing field and a total density (*i.e.* atomic plus molecular) of $2 \cdot 10^6 \text{ cm}^{-3}$ (Rizzo et al. 2003, and this paper). The main results are sketched in Fig. 7.

The molecules CO^+ , HOC^+ , C_2H , and C_3H_2 are known to be good tracers of the surface layers ($A_V < 5 \text{ mag}$) of the PDRs (see e.g. Sternberg & Dalgarno 1995). These environments are highly exposed to an intense UV field, and hence we will refer to these molecules as “*high UV*” species (HUV for brief). In particular, the reactive ion CO^+ is only expected to reach significant abundances at a visual extinction, $A_V < 2 \text{ mag}$ (Fuente et al. 2003; Rizzo et al. 2003). In Fig. 7a we show the CO^+ and HCO^+ fractional abundances as a function of the visual extinction for our model. As expected, the abundance of CO^+ is only significant at $A_V < 2 \text{ mag}$, and just at this low visual extinction, the predicted $[\text{CO}^+]/[\text{HCO}^+]$ ratio agrees with that measured in C2 towards the H II region (light gray region in Fig. 7a). The $[\text{CO}^+]/[\text{HCO}^+]$ ratio is more than one order of magnitude greater in C2 than in C1 (Table 4), which indicates that C1 arise in a more shielded layer of the molecular gas having $A_V > 4 \text{ mag}$ (dark gray region in Fig. 7a).

The $[\text{HCO}^+]/[\text{HOC}^+]$ ratio is a factor of 2 lower in C2 than in C1. Low values of the $[\text{HCO}^+]/[\text{HOC}^+]$ ratio are associated to highly ionized regions (Usero et al. 2004; Savage & Ziurys 2004; Fuente et al. 2005). Unfortunately, the reactive ion HOC^+ is not included in Le Bourlot’s model, but we can estimate its abundance in an indirect way. The $[\text{HCO}^+]/[\text{HOC}^+]$ ratio is strongly dependent on the electron abundance. In order to have $[\text{HCO}^+]/[\text{HOC}^+] \sim 450$, it is required an electron abundance, $X(e^-) > 2 \cdot 10^{-5}$ (Usero et al. 2004). Using our model, we conclude that these high electron abundances are only reached at $A_V < 4 \text{ mag}$. Thus, the $[\text{CO}^+]/[\text{HCO}^+]$ and the $[\text{HCO}^+]/[\text{HOC}^+]$ ratios support the interpretation of C2 as arising from a layer of molecular gas located at a visual extinction $< 4 \text{ mag}$ from the advancing ionization front. A new PDR model including reactions of HOC^+ is under development, and it will directly predict the $[\text{HCO}^+]/[\text{HOC}^+]$ ratio, as a function of global physical conditions (UV field, density, extinction) in a near future.

The $[\text{C}_3\text{H}_2]/[\text{C}_2\text{H}]$ ratio also changes between C1 and C2. In fact, this is a factor of 2–3 larger in C2 than in C1. Our chemical model predicts that the $[\text{C}_3\text{H}_2]/[\text{C}_2\text{H}]$ ratio is maximum at a visual extinction between 2 and 4 mag (see Fig. 7). These values of the visual extinction are in agreement with those derived from the measured $[\text{HCO}^+]/[\text{HOC}^+]$ ratio. Thus, it seems reasonable that the emission of C2 arises in the same layer of dense gas than HOC^+ ($A_V < 4 \text{ mag}$), while CO^+ arises in even a more external layer ($A_V < 2 \text{ mag}$). However, our model fails to predict values of $[\text{C}_3\text{H}_2]/[\text{C}_2\text{H}]$ as large as those measured in C2

even at this low visual extinction. The maximum value of the $[C_3H_2]/[C_2H]$ ratio predicted by the model is ~ 0.01 , three times lower than those measured in C2. (see Fig. 7b and Table 4). A failure of PDR models to account for the observed C_3H_2 abundance has already been commented in previous works (Fuente et al. 2003; Teyssier et al. 2004; Pety et al. 2005). The existence of an additional formation mechanism for C_3H_2 linked to the PAHs photodestruction has been proposed as an alternative to account the large C_3H_2 fractional abundances in PDRs.

Summarizing, we can infer from the comparison of our observations of HUV molecules and model calculations that C2 is tracing the dense molecular gas located at a visual extinction < 4 mag from the ionization front, while C1 is mainly tracing the more shielded part ($A_V > 5$ mag) of the PDR. Consequently, the UC H II region is surrounding by a thin layer ($< 4 \cdot 10^{21} \text{ cm}^{-2}$) of dense ($> 4 \cdot 10^6 \text{ cm}^{-3}$) molecular gas, whose chemistry is heavily affected by the UV stellar radiation and kinetically well represented by C2.

6.2. The back layers of the PDR: LUV species

In contrast to the HUV species, the column densities of HCO and SiO decrease towards the UC H II region, as expected in this harsh environment. Furthermore, their abundances are larger in C1 than in C2 (see $[HCO]/[H^{13}CO^+]$ and $[SiO]/[H^{13}CO^+]$ in Table 4), and show an enhancement at its edges (see Table 5).

Clearly, both HCO and SiO do not share a behavior similar to the HUV molecules; moreover, they are not particularly abundant in the cold envelope. Both molecules seem to be mainly present in the shielded parts of the PDR ($A_V > 5$ mag), and would belong to a family of species which can survive in those environments, less exposed to the UV field than the HUV molecules. We hereafter call such molecules as “*low UV*” (or LUV for briefing) species. The abundance of our LUV molecules are unusually high and could not be explained by gas-phase models (see, for example, Leung et al. 1984; Sternberg & Dalgarno 1995). Equally puzzling is the fact that both molecules peak at different positions.

As we have already stated before, both SiO and HCO have –near their maxima– abundances comparable to other PDRs, such as S140 and Orion Bar (Schilke et al. 2001). Moreover, the $[HCO]/[H^{13}CO^+]$ abundance ratio near the HCO peak is in the range 10–15, higher than in NGC 2024 (Schenewerk et al. 1988) and M82 (García-Burillo et al. 2002). This enhancement can be due to a few reasons. Firstly, some relevant chemical reactions leading to formation of SiO and HCO might not be considered in gas-phase models. It was already analyzed by several authors (see Walmsley et al. 1999; Schilke et al. 2001) and sounds rather

unlikely. Even though, we should not disregard the hypothesis, mainly due to a possible lack of complete chemical networks and rate coefficients.

So far, the most widely accepted alternative explanation arises by considering the grain chemistry. As many authors pointed out (see, for example, the review by Caselli 2005), the dust plays a key role in driving the chemistry and the energetics in PDRs. Walmsley et al. (1999) have modeled the Si chemistry in PDRs, and found that most of Si is in solid form at extinctions greater than 3 mag. This issue was observationally confirmed by Fuente et al. (2000) in NGC 7023, where a special distribution and enhancement of SiO was detected. Schilke et al. (2001) have included photodesorption of Si in their PDR model. SiO would later be produced in gaseous phase by reactions with OH and O₂. By doing so, those authors could account for the observed SiO abundance in Orion Bar and S140. Laboratory measurements of the rate coefficient of the reaction Si + O₂ → SiO + O (Le Picard et al. 2001), followed by detailed calculations of Si chemistry, have confirmed the results by Schilke et al. (2001).

In the case of HCO, the photodesorption of H₂CO –followed by its photodissociation in gaseous phase– have been claimed as a mechanism capable to counterbalance the photodissociation of HCO against the UV photons (Schilke et al. 2001). The authors could get an enhancement of HCO (at $A_V > 5$ mag) but not to the observed levels. This may be due to the need of more reliable rates for the processes involved, but also to the reduced network used in the gas-phase formation of this low-abundance species. We have measured similar abundances of HCO and hence are in a similar situation; the UV field intensity, greater in Mon R2 than in Orion Bar (Rizzo et al. 2003), does not seem to affect the HCO abundance.

However, photodesorption may not efficiently work in some other environments. Ruffle & Herbst (2001) have modeled both gas- and dust-chemistry in quiescent cores, and shown that the abundance of some species with lower binding energies than Si do not significantly change when including photodesorption. The modeled quiescent cores, however, have a G_0/n ratio at least two orders of magnitude lower than in Mon R2, because the densities are two orders of magnitude lower, and the incident UV field takes interstellar values. Even though, their results should be taken into account, and a complete model like the Ruffle & Herbst's one, under physical conditions more typical of PDRs, will surely improve our knowledge about the particular chemistry of LUV species and PDRs in general. Anyway, if SiO and HCO are formed after photodesorption of Si and H₂CO, respectively, we would expect other atoms and molecules do so, and would be detectable. At this respect, an interesting test may be to carry out an observational campaign to search for and study other LUV species throughout the whole field. A good candidate to belong to the LUV group in NH₃, a widely recognized species linked to grain chemistry, whose abundance close to the borders of H II regions is enhanced (Larsson et al. 2003).

The different spatial distributions of our LUV molecules is another interesting issue. Both molecules almost complete a “ring” between the UC H II region and the molecular envelope. However, they peak at different locations throughout the ring: while SiO arises in the densest part of the ionization front, HCO peaks in the tail of the cometary shape. Different local conditions should exist in order to explain the variations in relative abundances of SiO and HCO. A rather simple explanation is that HCO and SiO have a different desorption yield; in this case one would expect a layered structure in the morphology of these molecules. Unfortunately, the low angular resolution of the HCO and SiO maps prevent us from concluding about that. A second possibility is that a low-velocity shock associated with the ionization front contributes to enhance the HCO and/or SiO abundances. In the case of hot cores, this process was already analyzed by Viti et al. (2001). The low velocity shocks contribute to release Si and/or H₂CO from the grain surfaces, and the gas phase chemistry is modified by the advancing shock front. The radical HCO is rapidly destroyed by O, but in shocked regions the O abundance is reduced because it is converted to H₂O. Furthermore, SiO is efficiently formed by the reaction Si + OH → SiO + H, being OH the photodissociation product of H₂O. Thus, the HCO and SiO abundances are very sensitive to the O/OH/H₂O relative fractional abundances and can change locally because of low velocity shocks and small inhomogeneities in the incident UV field. Finally, a variation in the grain composition may account for the differences between the HCO-peak to the SiO-peak.

Observations of dust emission may help to solve this interesting puzzle in Mon R2. Kraemer et al. (2001) have studied this region in the mid-IR, from 8.2 to 20.6 μ m. Besides the IR sources, continuum dust emission is dominated by a ring-like structure which roughly bounds the ionized region. While the dust temperature is rather uniform in the area (100–115 K), the opacity is greater in the ring. Kraemer et al. (2001) also studied the silicate absorption feature at 10 μ m, and found a patchy distribution, not necessarily correlated to the point sources, the temperature, or the opacity. So far, dust properties may significantly change in areas as small as a few arcsec. Although this result encourages one of our alternatives (variation in grain composition), the distribution of HCO and SiO is still an open subject because the other proposed explanations (different desorption yield and low-velocity shocks) may be working in this case.

To summarize, our SiO and HCO observations show that these compounds are enhanced in the outskirts of the UC H II regions ($A_V > 5$ mag). The enhancement in the abundance of these species may be related to the interaction of the UV photons with grains, instead of the direct effect of the UV photons on the molecular gas chemistry. The interaction of the UV photons with grains may modify the chemistry of large column densities of the molecular gas, and may show an evidence of the advancing PDR into the molecular cloud.

7. On the kinematics of the dense gas layer

In the UC H II regions, the high densities of the ionized gas lead to enormous internal pressures ($nT \sim 10^9 \text{ cm}^{-3} \text{ K}$). Since the sources are very small, their expansion timescales should be as short as a few hundred years (Dreher & Welch 1981). Surprisingly, the number of UC H II regions is greater than the expected from the massive star formation rate (Wood & Churchwell 1989), which is known as the “lifetime problem” of the UC H II regions. A deep knowledge of the morphology and physical conditions of the dense PDR around the UC H II region in Mon R2, would shed some light on this problem. We can explore one of the proposed explanations, in which the extremely dense neutral gas confine the H II region by pressure (de Pree et al. 1995; Akeson & Carlstrom 1996); our data show the existence of a gas layer with $n(\text{H}_2) > 4 \cdot 10^6 \text{ cm}^{-3}$. Hence, if we assume a kinetic temperature of 100 K, a hydrogen density $n(\text{H}_2) \sim 10^7 \text{ cm}^{-3}$ would be enough to pressure-confine the UC H II region.

The velocity range associated to C2 is undoubtedly different from that linked to the parent molecular cloud, and hence it should have a particular kinematics. By means of the PDR chemistry, we have a good chance of further studying the kinematics of the molecular gas confining the UC H II region, because some chemical species may avoid the confusion of the foreground molecular cloud. In Fig. 8, we show the position-velocity (P-V) diagram of the C_3H_2 2→1 (Fig. 8a) and 6→5 lines (Fig. 8b) across the observed strip. As we previously discussed, most of the C_3H_2 2→1 line traces C1, whereas the 6→5 emission is dominated by C2. The P-V diagram of the C_3H_2 6→5 line is preferably located toward the H II region (center of the map), rather than extended along the whole strip. The curves superimposed in Fig. 8 were symmetrically traced around C1, and roughly follow the C_3H_2 6→5 maxima. As the extreme velocities of the curves are ≈ 7 and 12 km s^{-1} , this pattern is compatible with a picture where the PDR is expanding at a velocity between 2 and 3 km s^{-1} . It is worth mentioning that such a low expansion velocity was recently observed in an UC H II region in W48, by observations of carbon recombination lines (Roshi et al. 2005).

8. Conclusions

We have carried out a molecular survey towards the UC H II region Mon R2 to have a deeper insight into the chemistry associated to this kind of objects. Our results show the existence of two groups of molecules. The first group (HUV) is formed by molecules that present large abundances in the surface layers of PDRs ($A_V < 5 \text{ mag}$). The species CO^+ , HOC^+ , C_2H , and C_3H_2 belong to this group. Gas-phase PDR models can successfully account for the behavior of CO^+ , HOC^+ , and C_2H . In the case of C_3H_2 , however, PDR models fall short of explaining the observed abundances. New C_3H_2 formation mechanisms

linked to the photodestruction of PAHs have been proposed to account for this difference.

HCO and SiO belong to another group of molecules (LUV). Their abundances are enhanced at the edges of the PDR ($A_V > 5$ mag), which cannot be explained by current gas-phase PDR models. Photodesorption from grain mantles appears like a probable mechanism capable of explaining the observed abundances. A revision of gas-phase chemical networks, as well as a model able to include photodesorption in PDRs, may significantly improve the knowledge of LUV species. Other molecules, like NH₃, whose chemistry is related with the grains also present large abundances at the edges of the H II regions (Larsson et al. 2003). This issue may show that the interactions of the UV radiation with the grains could produce important effects on the chemistry of the molecular gas, even at local visual extinction as deep as 10 mag.

Finally, we have used PDR chemistry to determine the physical conditions and kinematics of the layer of gas surrounding the UC H II region. Using a LVG code to fit our C₃H₂ observations, we have derived hydrogen densities $> 4 \cdot 10^6 \text{ cm}^{-3}$ for this layer. The proposed scenario of a pressure-confined H II region requires $n(\text{H}_2) \sim 10^7 \text{ cm}^{-3}$, perfectly compatible with this result. In addition, the P-V diagram of the C₃H₂ lines might show that while the gas layers at a visual extinction < 5 mag are expanding at a velocity of $\sim 2\text{--}3 \text{ km s}^{-1}$, the back layers of the PDR are moving at the velocities of the foreground molecular cloud. This kinematics supports the interpretation that the UC H II region could be confined by a dense ($n(\text{H}_2) > 10^6 \text{ cm}^{-3}$) and thin ($< 4 \cdot 10^{21} \text{ cm}^{-2}$) layer of neutral gas.

On the other hand, the search for other LUV molecules looks as an exciting observational task which may lead to determine the chemical processes carrying out in the more shielded part of PDRs. Moreover, further observations and multi-transitional studies of the HUV molecules are needed to determine accurately the physical conditions and dynamics of this neutral layer.

We are grateful to the technical staff in Pico de Veleta for their professional support during the observations. We specially wish to thank the anonymous referee, who greatly improved the paper by sharing with us his/her viewpoints about the PDR chemistry. This paper has been partially funded by the Spanish MCyT under projects DGES/AYA2000-927, ESP2001-4519-PE, ESP2002-01693, and AYA2003-06473.

Facilities: IRAM(MRT-30m).

REFERENCES

- Akeson, R. L., & Carlstrom, J. E. 1996, *ApJ*, 470, 528
- Caselli, P. 2005, Proceedings of the meeting “Cores to clusters”, Porto, Portugal (*astro-ph/0504298*)
- Chandra, S. 2003, *A&A*, 402, 1
- Chandra, S., & Kegel, W. H. 2000, *A&AS*, 142, 113
- Choi, M., Evans, N. J., Tafalla, M., & Bachiller, R. 2000, *ApJ*, 538, 738
- de Pree, C. G., Rodriguez, L. F., Dickel, H. R., & Goss, W. M. 1995, *ApJ*, 447, 220
- Dreher, J. W., & Welch, W. J. 1981, *ApJ*, 245, 857
- Fuente, A., García-Burillo, S., Gerin, M., Teyssier, D., Usero, A., Rizzo, J. R., & de Vicente, P. 2005, *ApJ*, 619, L155
- Fuente, A., Martín-Pintado, J., Rodríguez-Fernández, N. J., Cernicharo, J., & Gerin, M. 2000, *A&A*, 354, 1053
- Fuente, A., Rodríguez-Franco, A., García-Burillo, S., Martín-Pintado, J., & Black, J. H. 2003, *A&A*, 406, 899
- García-Burillo, S., Martín-Pintado, J., Fuente, A., & Neri, R. 2000, *A&A*, 355, 499
- García-Burillo, S., Martín-Pintado, J., Fuente, A., & Neri, R. 2001, *ApJ*, 563, L27
- García-Burillo, S., Martín-Pintado, J., Fuente, A., Usero, A., & Neri, R. 2002, *ApJ*, 575, L55
- Giannakopoulou, J., Mitchell, G. F., Hasegawa, T. I., Matthews, H. E., & Maillard, J. 1997, *ApJ*, 487, 346
- Green, S., & Thaddeus, P. 1974, *ApJ*, 191, 653
- Henning, T., Chini, R., & Pfau, W. 1992, *A&A*, 263, 285
- Herbst, W. & Racine, R. 1976, *AJ*, 81, 840
- Jaffe, D. T., Zhu, Q., Lacy, J. H., & Richter, M. 2003, *ApJ*, 596, 1053
- Kraemer, K. E., Jackson, J. M., Deutsch, L. K., Kassis, M., Hora, J. L., Fazio, G. G., Hoffmann, W. F., & Dayal, A. 2001, *ApJ*, 561, 282

- Larsson, B., et al. 2003, A&A, 402, L69
- Le Bourlot, J., Pineau des Forêts, G., Roueff, E., & Flower, D. R. 1993, A&A, 267, 233
- Le Picard, S. D., Canosa, A., Pineau des Forêts, G., Rebrion-Rowe, C., & Rowe, B. R. 2001, A&A, 372, 1064
- Leung, C. M., Herbst, E., & Huebner, W. F. 1984, ApJS, 56, 231
- Martín-Pintado, J., de Vicente, P., Fuente, A., & Planesas, P. 1997, ApJ, 482, L45
- Massi, M., Felli, M., & Simon, M. 1985, A&A, 152, 387
- Meyers-Rice, B. A. & Lada, C. J. 1991, ApJ, 368, 445
- Pety, J., Teyssier, D., Fossé, D., Gerin, M., Roueff, E., Abergel, A., Habart, E., & Cernicharo, J. 2005, A&A, 435, 885
- Rizzo, J. R., Fuente, A., Rodríguez-Franco, A., & García-Burillo, S. 2003, ApJ, 597, L153
- Rodríguez-Franco, A., Martín-Pintado, J., & Fuente, A. 1998, A&A, 329, 1097
- Roshi, D. A., Goss, W. M., Anantharamaiah, K. R., & Jeyakumar, S. 2005, ApJ, 626, 253
- Ruffle, D. P., & Herbst, E. 2001, MNRAS, 322, 770
- Savage, C., & Ziurys, L. M. 2004, ApJ, 616, 966
- Schenewerk, M. S., Jewell, P. R., Snyder, L. E., Hollis, J. M., & Ziurys, L. M. 1988, ApJ, 328, 785
- Schilke, P., Pineau des Forêts, G., Walmsley, C. M., & Martín-Pintado, J. 2001, A&A, 372, 291
- Seaquist, E. R., Carlstrom, J. E., Bryant, P. M., & Bell, M. B. 1996, ApJ, 465, 691
- Sternberg, A., & Dalgarno, A. 1995, ApJS, 99, 565
- Teyssier, D., Fossé, D., Gerin, M., Pety, J., Abergel, A., & Roueff, E. 2004, A&A, 417, 135
- Truong-Bach, Nguyen-Q-Rieu, Omont, A., Olofsson, H., & Johansson, L. E. B. 1987, A&A, 176, 285
- Usero, A., García-Burillo, S., Fuente, A., Martín-Pintado, J., & Rodríguez-Fernández, N. J. 2004, A&A, 419, 897

- Viti, S., Caselli, P., Hartquist, T. W., & Williams, D. A. 2001, A&A, 370, 1017
Walmsley, C. M., Pineau des Forêts, G., & Flower, D. R. 1999, A&A, 342, 542
Wood, D. O. S. & Churchwell, E. 1989, ApJS, 69, 831

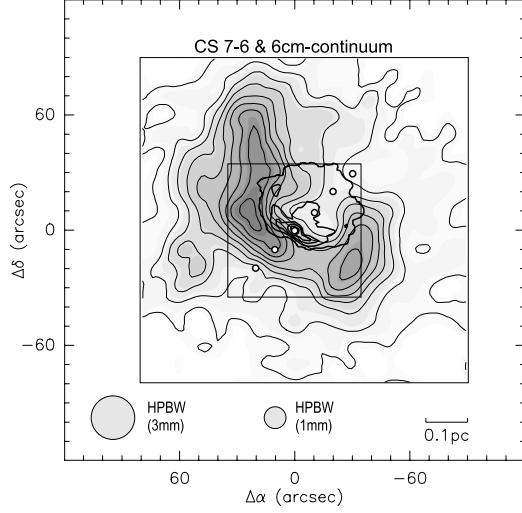


Fig. 1.— Location of the positions observed in this paper. Greyscale represent the CS $7 \rightarrow 6$ line emission map from Choi et al. (2000). The circles across the symmetry axis of the UC HII region indicate the positions observed in the C_3H_2 and C_2H lines. The small square, $72'' \times 72''$ in size, traces the mapped area in HC_3N , H^{13}CO^+ , SiO , and HCO .

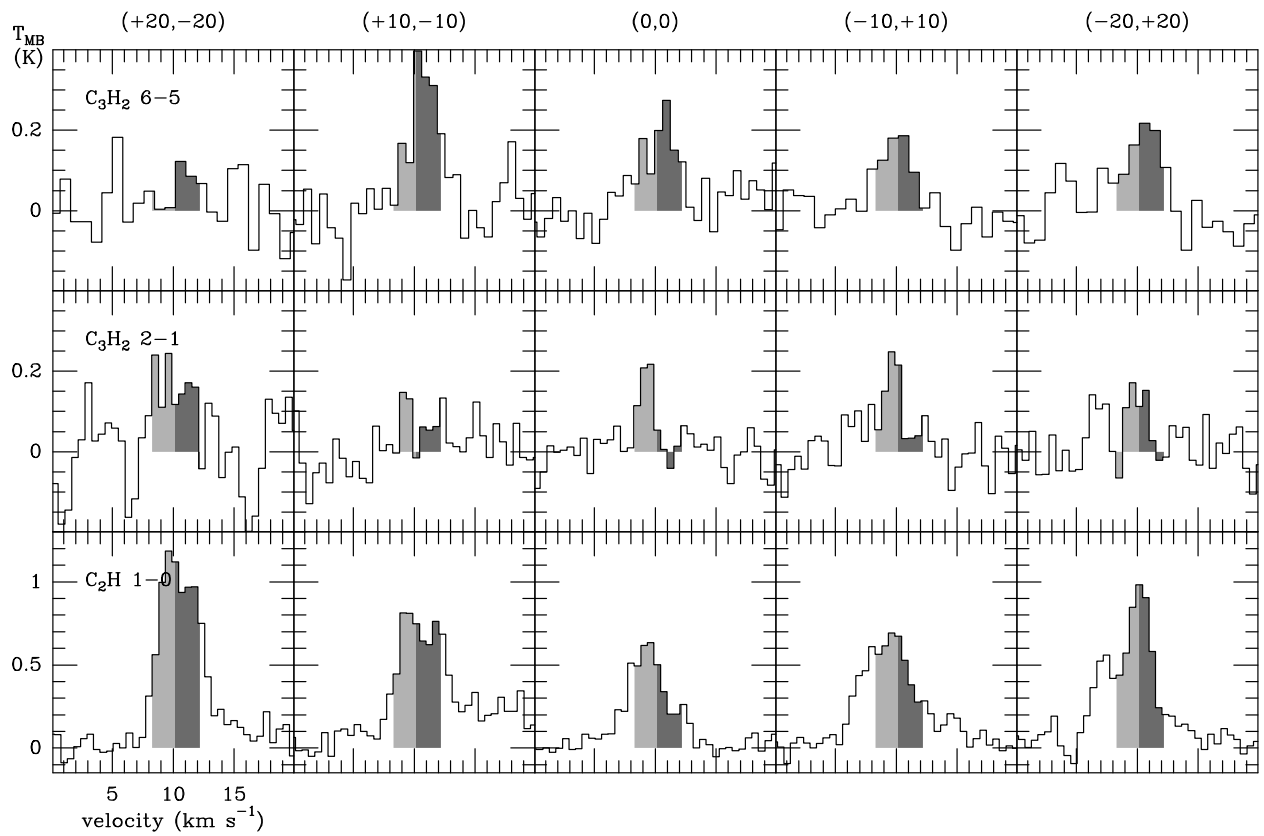


Fig. 2.— A sample of C_3H_2 6→5 (a), C_3H_2 2→1 (b), and C_2H 1→0 (c) spectra along the strip. The positions are indicated at the top part of the figure. The shadowed areas indicate the approximate velocity extension of the two kinematic component present in the region.

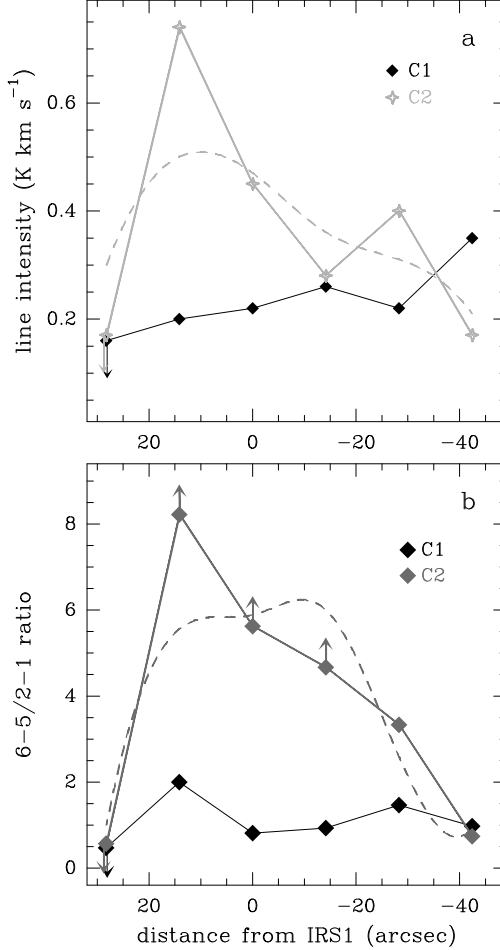


Fig. 3.— C₃H₂ observed parameters along the strip, for each of the velocity components defined in the text. (a) C₃H₂ 6→5 line intensity. (b) C₃H₂ 6→5 to 2→1 line ratio. Note the uniformity of the C1 component and the separation of both components in Fig. b. The dashed curves are the corresponding to the C2 component, after smoothing the 6→5 line to the resolution of the 2→1 line. Angular distances are referred to Mon R2 IRS 1, increasing toward the southeast.

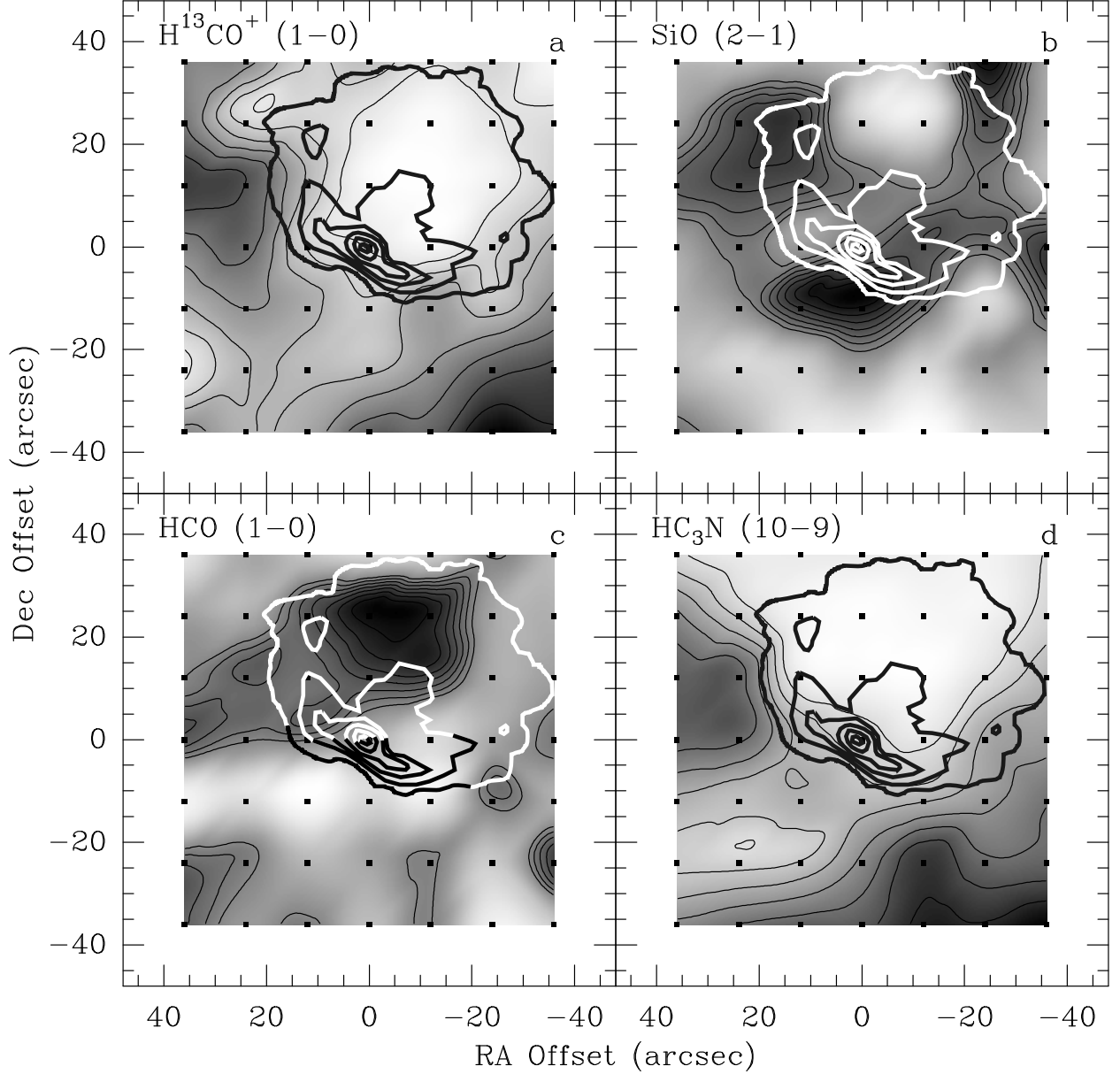


Fig. 4.— Emission maps around the UC HII region Mon R2. The mapped rotational lines are indicated in the top left corner of each map. Contour levels are 30% to 90% of the map peak, in steps of 10%. The map peaks are 2.265, 0.243, 0.244, and 3.651 K km s^{-1} for maps **a** to **d**, respectively. Superimposed are the 6 cm-continuum emission from Wood & Churchwell (1989).

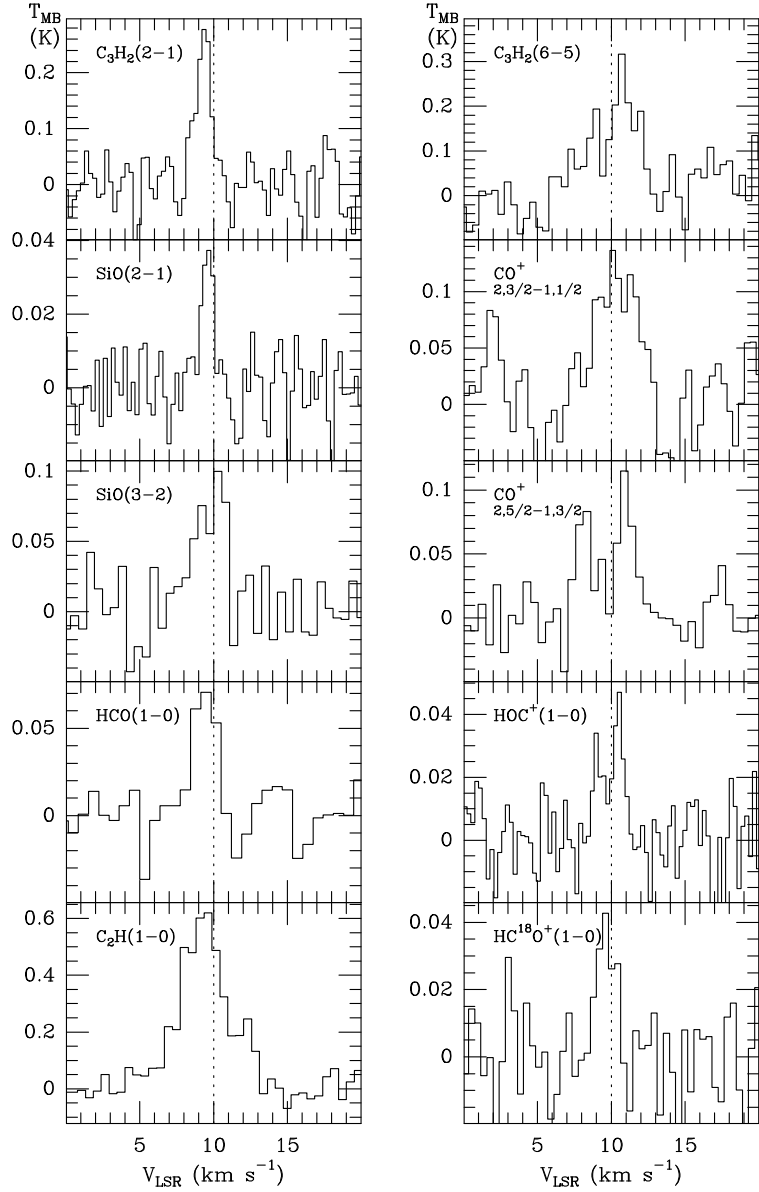


Fig. 5.— Spectra toward the position $(0'', 0'')$. The rotational transition observed is indicated. Temperature scale is T_{MB} , in K. There are two types of emission depending on the velocity range, roughly in agreement with the velocity components defined in Sect. 3. The emission below 10 km s^{-1} is associated to the molecular envelope (component 1), while the emission above 10 km s^{-1} is linked to the ultracompact H II region (component 2).

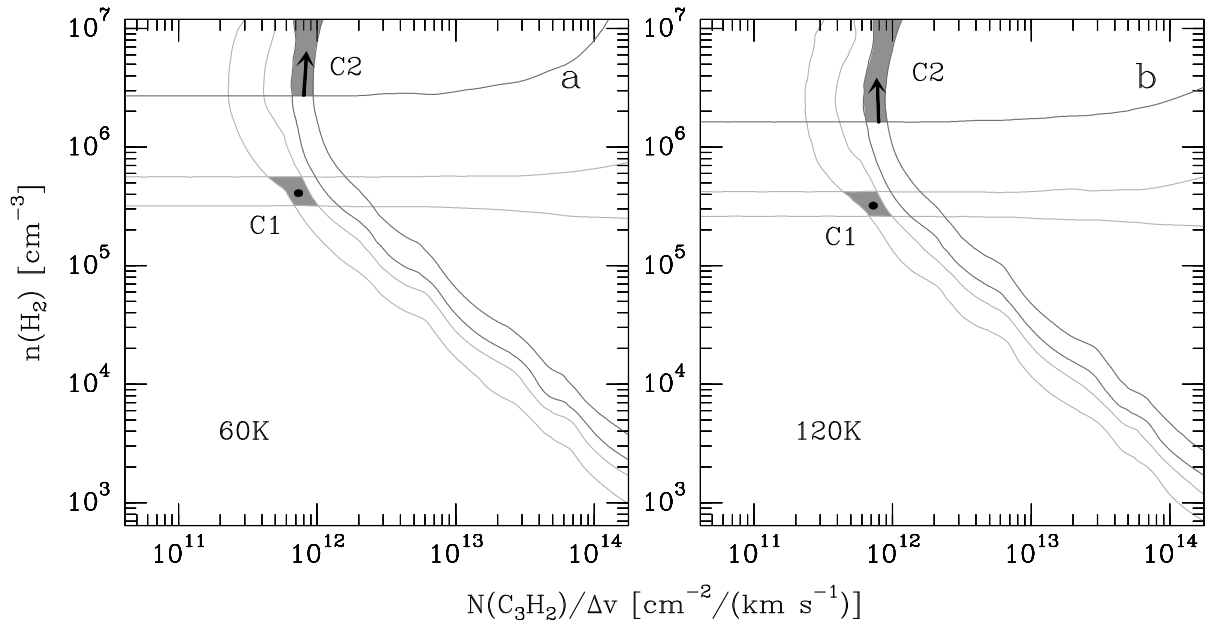


Fig. 6.— LVG results at the (0'',0'') position, for kinetic temperatures of (a) 60 K and (b) 120 K. For each component, it is plotted the observed values of the C_3H_2 6 \rightarrow 5 line intensity (vertical/diagonal lines), as well as the C_3H_2 [6 \rightarrow 5]/[2 \rightarrow 1] line ratio (horizontal lines), as functions of the C_3H_2 column density and the H_2 density. Shadowed areas take into account the observational errors. Although both components have comparable column densities, the C1 density is lower than that corresponding to C2 at least by a factor of four.

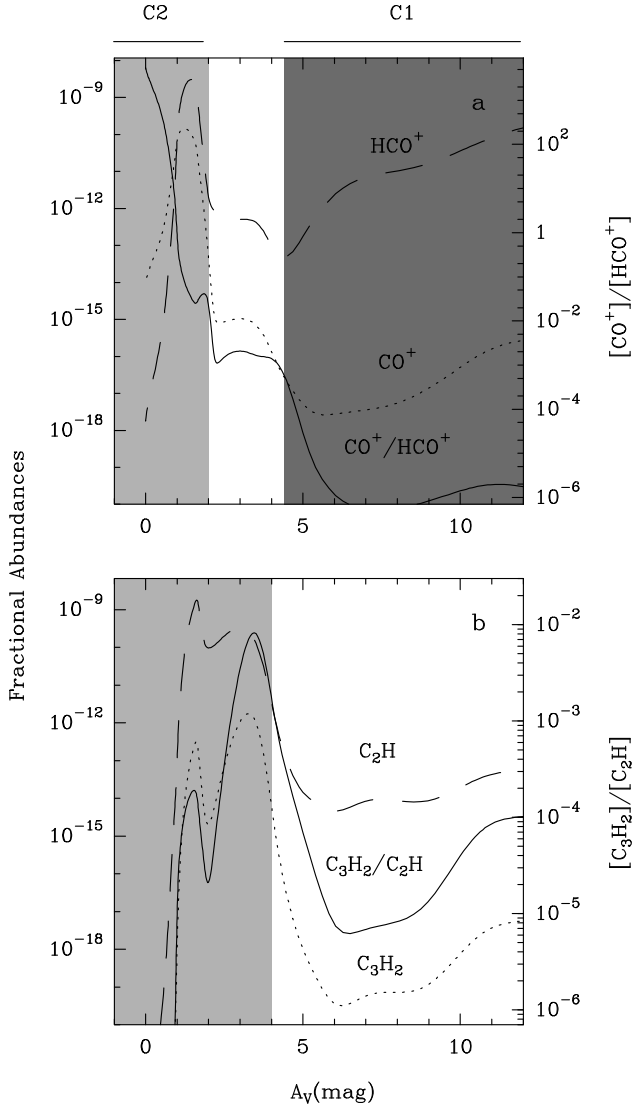


Fig. 7.— Model predictions for the abundances of various species derived from updated Le Bourlot et al.’s model. The calculations have been carried out for $n(\text{H}_2)=2\ 10^6\ \text{cm}^{-3}$ and $G_0=5\ 10^5$ in units of the Habing field. (a) CO^+ and HCO^+ fractional abundances. CO^+ is significantly abundant at visual extinctions around 2 mag, indicated by the light gray area, which roughly corresponds to the values measured in C2. On the other hand, the dark gray area agrees with the upper limits of the $[\text{CO}^+/\text{HCO}^+]$ ratio measured in C1. (b) C_3H_2 and C_2H fractional abundances, as a function of the visual extinction. The $[\text{C}_3\text{H}_2]/[\text{C}_2\text{H}]$ ratio peaks between 2 and 5 mag (gray areas).

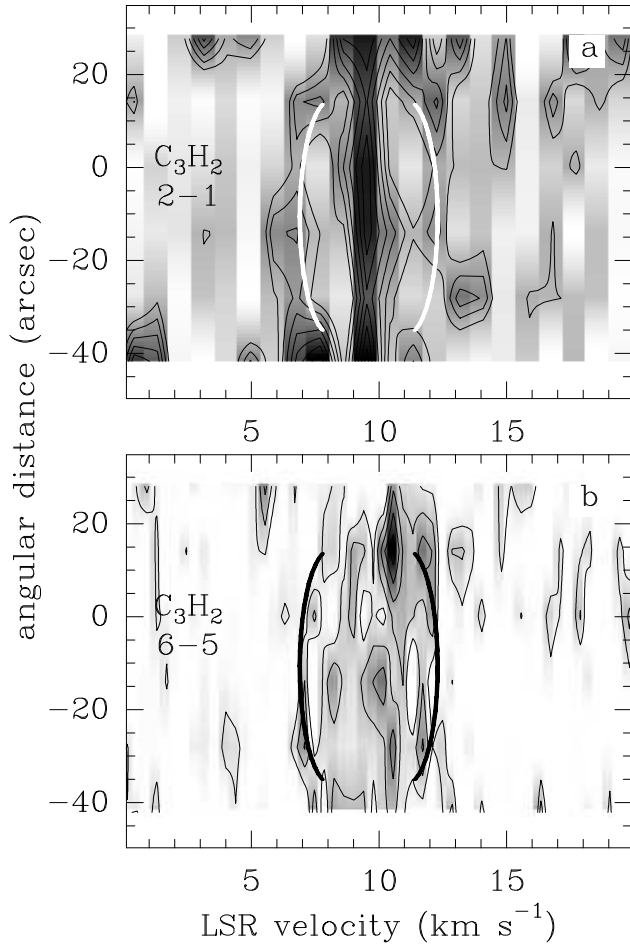


Fig. 8.— Position-velocity diagram of (a) C₃H₂ 2→1 and (b) C₃H₂ 6→5 lines across the strip. Angular distances are referred to Mon R2 IRS1, increasing toward the southeast. Most of the C₃H₂ 2→1 emission arises from the C1 component, between 9 and 10 km s⁻¹. The curves roughly follow the maxima at high velocities, which includes the C2 component. This pattern is compatible with an expansion of 2–3 km s⁻¹

Table 1. Observing frequencies and telescope parameters

Molecule	Transition	Freq (GHz)	beam	η_{MB}
C ₂ H	$N = 1 - 0, J = 3/2 - 1/2$			
	$F = 1 \rightarrow 1$	87.284156	28.5''	0.77
	$F = 2 \rightarrow 1$	87.316925	28.5''	0.77
	$F = 1 \rightarrow 0$	87.328624	28.5''	0.77
C ₃ H ₂	$J(K_a, K_c) =$			
	2(1,2) \rightarrow 1(0,1)	85.338893	29''	0.77
	3(2,2) \rightarrow 2(1,1)	155.518295	17''	0.65
	6(0,6) \rightarrow 5(1,5)	217.822148	11.5''	0.52
	6(1,6) \rightarrow 5(0,5)	217.822148	11.5''	0.52
	5(1,4) \rightarrow 4(2,3)	217.940046	11.5''	0.52
HC ₃ N	$J = 10 \rightarrow 9$	90.9789933	27''	0.76
HCO	$N_{K-K+} = 1_{01} - 0_{00}$			
	$J = 3/2 - 1/2, F = 2 \rightarrow 1$	86.6708200	28.5''	0.77
SiO	$J = 2 \rightarrow 1$	86.8468910	28.5''	0.77
SiO	$J = 3 \rightarrow 2$	130.268702	19''	0.70
H ¹³ CO ⁺	$J = 1 \rightarrow 0$	86.7543300	28.5''	0.77

Table 2. One-component Gaussian fits to the C₃H₂ and C₂H spectral lines

Offset arcsec	Line	Area K km s ⁻¹	V _{LSR} km s ⁻¹	ΔV _{1/2} km s ⁻¹
(20, -20)	C ₃ H ₂ 6 → 5 ^a	< 0.13
(10, -10)	C ₃ H ₂ 6 → 5 ^a	1.10 (0.10)	10.9 (0.1)	2.8 (0.3)
(0, 0)	C ₃ H ₂ 6 → 5 ^a	0.82 (0.11)	10.4 (0.2)	3.7 (0.6)
(-10, +10)	C ₃ H ₂ 6 → 5 ^a	0.76 (0.10)	9.8 (0.2)	3.6 (0.6)
(-20, +20)	C ₃ H ₂ 6 → 5 ^a	0.76 (0.15)	10.5 (0.3)	3.3 (0.8)
(-30, +30)	C ₃ H ₂ 6 → 5 ^a	0.70 (0.14)	9.5 (0.3)	2.7 (0.5)
(20, -20)	C ₃ H ₂ 5(1, 4) → 4(2, 3)	< 0.07
(10, -10)	C ₃ H ₂ 5(1, 4) → 4(2, 3)	0.76 (0.09)	10.6 (0.3)	3.4 (0.5)
(0, 0)	C ₃ H ₂ 5(1, 4) → 4(2, 3)	0.56 (0.07)	8.9 (0.3)	4.2 (0.6)
(-10, +10)	C ₃ H ₂ 5(1, 4) → 4(2, 3)	0.47 (0.12)	10.6 (0.6)	4.4 (1.2)
(-20, +20)	C ₃ H ₂ 5(1, 4) → 4(2, 3)	< 0.06
(-30, +30)	C ₃ H ₂ 5(1, 4) → 4(2, 3)	< 0.06
(20, -20)	C ₃ H ₂ 3(2, 2) → 2(1, 1)	< 0.11
(10, -10)	C ₃ H ₂ 3(2, 2) → 2(1, 1)	0.18 (0.04)	11.6 (0.1)	0.5 (0.2)
(0, 0)	C ₃ H ₂ 3(2, 2) → 2(1, 1)	0.38 (0.09)	9.8 (0.7)	5.6 (1.3)
(-10, +10)	C ₃ H ₂ 3(2, 2) → 2(1, 1)	< 0.09
(-20, +20)	C ₃ H ₂ 3(2, 2) → 2(1, 1)	< 0.11
(-30, +30)	C ₃ H ₂ 3(2, 2) → 2(1, 1)	< 0.15
(20, -20)	C ₃ H ₂ 2(1, 2) → 1(0, 1)	0.62 (0.20)	9.9 (0.6)	3.3 (1.1)
(10, -10)	C ₃ H ₂ 2(1, 2) → 1(0, 1)	< 0.11
(0, 0)	C ₃ H ₂ 2(1, 2) → 1(0, 1)	0.29 (0.04)	9.3 (0.1)	1.1 (0.2)
(-10, +10)	C ₃ H ₂ 2(1, 2) → 1(0, 1)	0.41 (0.09)	9.7 (0.2)	1.6 (0.6)
(-20, +20)	C ₃ H ₂ 2(1, 2) → 1(0, 1)	0.25 (0.09)	9.8 (0.3)	1.8 (0.7)
(-30, +30)	C ₃ H ₂ 2(1, 2) → 1(0, 1)	1.09 (0.17)	8.4 (0.4)	4.6 (0.7)
(20, -20)	C ₂ H 1 → 0	4.77 (0.18)	10.5 (0.1)	3.9 (0.2)
(10, -10)	C ₂ H 1 → 0	3.49 (0.03)	10.7 (0.2)	4.7 (0.3)

Table 2—Continued

Offset arcsec	Line	Area K km s ⁻¹	V _{LSR} km s ⁻¹	ΔV _{1/2} km s ⁻¹
(0, 0)	C ₂ H 1 → 0	2.32 (0.12)	9.3 (0.1)	3.8 (0.3)
(-10, +10)	C ₂ H 1 → 0	3.67 (0.10)	9.3 (0.1)	5.3 (0.2)
(-20, +20)	C ₂ H 1 → 0	3.57 (0.18)	9.7 (0.1)	4.5 (0.3)
(-30, +30)	C ₂ H 1 → 0	1.97 (0.23)	10.3 (0.1)	2.7 (0.5)

Note. — Number in parenthesis are 3σ errors in each parameter.

^aParameters correspond to the transitions 6(1, 6) → 5(0, 5) and 6(0, 6) → 5(1, 5) together, which are blended at the same frequency.

Table 3. LVG results for C_3H_2 and C_2H

Offset ('', '')	Component 1		Component 2		$N(\text{C}_2\text{H})$ 10^{14} cm^{-2}	$\frac{[\text{C}_3\text{H}_2]}{[\text{C}_2\text{H}]}$ ^a
	$n(\text{H}_2)$ cm^{-3}	$N(\text{C}_3\text{H}_2)$ 10^{12} cm^{-2}	$n(\text{H}_2)$ cm^{-3}	$N(\text{C}_3\text{H}_2)$ 10^{12} cm^{-2}		
(+20, -20)	$<2.4 \cdot 10^5$	$\lesssim 2.2$	$<4.6 \cdot 10^5$	$\lesssim 1.8$	4.2	0.010
(+10, -10)	$8.4 \cdot 10^5$	1.1	$>3.5 \cdot 10^6$	4.0	3.0	0.017
(0, 0)	$4.5 \cdot 10^5$	1.8	$>4.5 \cdot 10^6$	2.3	2.0	0.021
(-10, +10)	$4.6 \cdot 10^5$	2.2	$>4.7 \cdot 10^6$	1.4	3.2	0.011
(-20, +20)	$6.4 \cdot 10^5$	1.6	$1.1 \cdot 10^6$	2.4	3.1	0.013
(-30, +30)	$4.5 \cdot 10^5$	3.1	$4.4 \cdot 10^5$	1.8	1.7	0.029

Note. — Assumed a kinetic temperature of 50 K. C_2H was not separated by components.

^aThe $\frac{[\text{C}_3\text{H}_2]}{[\text{C}_2\text{H}]}$ abundance ratio involves the whole emission from the two molecules.

Table 4. Column densities and relative abundances

Molecule/ratio	unit	C1(10,-10)	C2(10,-10)	C1(0,0)	C2(0,0)
C_3H_2	10^{12} cm^{-2}	1.1	4.0	1.8	2.3
C_2H	10^{14} cm^{-2}	1.4	1.5	1.2	0.8
CO^+	10^{10} cm^{-2}	< 4.8	< 5.2	< 4.8	31.1
HOC^+	10^{10} cm^{-2}	< 2.6	9.9	8.8	9.6
HCO	10^{12} cm^{-2}	< 3.6	< 3.9	3.7	< 1.2
H^{13}CO^+	10^{11} cm^{-2}	9.3	9.5	5.9	5.8
HC_3N	10^{12} cm^{-2}	2.0	5.2	1.1	4.0
SiO	10^{10} cm^{-2}	34	< 22	11	< 1.6
HC^{18}O^+	10^{10} cm^{-2}	10.9	14.2	11.3	6.6
$\text{HCO}^+/\text{HOC}^+$		> 2700	930	830	450
CO^+/HCO^+	10^{-4}	< 7	< 6	< 7	72
$\text{C}_3\text{H}_2/\text{C}_2\text{H}$	10^{-3}	8	26	15	30
$\text{C}_3\text{H}_2/\text{HC}_3\text{N}$		0.6	0.8	1.6	0.6
$\text{HCO}/\text{H}^{13}\text{CO}^+$		< 3.9	< 4.1	6.3	< 2.1
$\text{SiO}/\text{H}^{13}\text{CO}^+$		0.37	< 0.23	0.19	< 0.03

Table 5. Column densities and abundances at selected positions

Position (",'")	$N(\text{HCO})$ 10^{12} cm^{-2}	$N(\text{H}^{13}\text{CO}^+)$ 10^{12} cm^{-2}	$N(\text{HC}_3\text{N})$ 10^{12} cm^{-2}	$N(\text{SiO})$ 10^{11} cm^{-2}	$\frac{[\text{HCO}]}{[\text{H}^{13}\text{CO}^+]}$	$\frac{[\text{HCO}]}{[\text{HC}_3\text{N}]}$	$\frac{[\text{HCO}]}{[\text{SiO}]}$	Comment
(+12, +24)	15.8	1.7	6.4	< 2.2	9.3	2.5	> 720	HCO peak
(0, +24)	14.1	1.0	4.1	< 2.2	14.7	3.4	> 640	HCO peak
(0, 0)	< 2.5	1.6	11.9	0.8	< 1.6	< 0.2	< 310	center
(+12, -12)	< 3.7	1.7	11.1	4.3	< 2.2	< 0.3	< 90	SiO peak
(+36, +12)	4.0	2.8	18.9	< 2.0	1.4	0.2	> 200	Dense envelope
(-12, -36)	9.6	1.8	25.6	< 1.6	5.3	0.4	> 600	Dense envelope
(0, -12)	< 3.1	1.3	12.0	6.0	< 2.4	< 0.3	< 50	SiO peak